

# Measurement of Medial Elbow Joint Space using Landmark Detection

Shizuka Akahori<sup>1\*</sup>, Shotaro Teruya<sup>2</sup>, Pragyan Shrestha<sup>1</sup>,  
Yuichi Yoshii<sup>3</sup>, Ryuhei Michinobu<sup>4</sup>, Satoshi Iizuka<sup>5</sup>,  
Itaru Kitahara<sup>5</sup>

<sup>1\*</sup>Graduate School of Science and Technology, University of Tsukuba,  
1-1-1 Tennodai, Tsukuba, 305-8571, Ibaraki, Japan.

<sup>2\*</sup>Department of Orthopaedic Surgery, University of Tsukuba, 1-1-1  
Tennodai, Tsukuba, 305-8571, Ibaraki, Japan.

<sup>3</sup>Department of Orthopaedic Surgery, Ibaraki Medical Center, Tokyo  
Medical University, 3-20-1 Ami, Inashiki, 300-0332, Ibaraki, Japan.

<sup>4\*</sup>, Tsukuba Wellness Orthopaedics, 2011-54 Sasagi, Tsukuba, 305-0043 ,  
Ibaraki, Japan.

<sup>5\*</sup>Institute of Systems and Information Engineering, University of  
Tsukuba, 1-1-1 Tennodai, Tsukuba, 305-8571, Ibaraki, Japan.

\*Corresponding author(s). E-mail(s):

[akahori.shizuka@image.iit.tsukuba.ac.jp](mailto:akahori.shizuka@image.iit.tsukuba.ac.jp);

Contributing authors: [steruya@tsukuba-seikei.jp](mailto:steruya@tsukuba-seikei.jp);

[shrestha.pragyan@image.iit.tsukuba.ac.jp](mailto:shrestha.pragyan@image.iit.tsukuba.ac.jp); [yyoshii@tsukuba-seikei.jp](mailto:yyoshii@tsukuba-seikei.jp);

[michinobu@tsukuba-seikei.jp](mailto:michinobu@tsukuba-seikei.jp); [iizuka@cs.tsukuba.ac.jp](mailto:iizuka@cs.tsukuba.ac.jp);

[kitahara@ccs.tsukuba.ac.jp](mailto:kitahara@ccs.tsukuba.ac.jp);

## Abstract

Ultrasound imaging of the medial elbow is crucial for the early diagnosis of Ulnar Collateral Ligament (UCL) injuries. Specifically, measuring the elbow joint space in ultrasound images is used to assess the valgus instability of the elbow caused by UCL injuries. To automate this measurement, a model trained on a precisely annotated dataset is necessary; however, no publicly available dataset exists to date. This study introduces a novel ultrasound medial elbow dataset to measure the joint space. The dataset comprises 4,201 medial elbow ultrasound images from 22 subjects, with landmark annotations on the humerus and ulna, based

on the expertise of three orthopedic surgeons. We evaluated joint space measurement methods on our proposed dataset using heatmap-based, regression-based, and token-based landmark detection methods. While heatmap-based landmark detection methods generally achieve high accuracy, they sometimes produce multiple peaks on a heatmap, leading to incorrect detection. To mitigate this issue and enhance landmark localization, we propose Shape Subspace (SS) landmark refinement by measuring geometrical similarities between the detected and reference landmark positions. The results show that the mean joint space measurement error is 0.116 mm when using HRNet. Furthermore, SS landmark refinement can reduce the mean absolute error of landmark positions by 0.010 mm with HRNet and by 0.103 mm with ViTPose on average. These highlight the potential for high-precision, real-time diagnosis of UCL injuries by accurately measuring joint space. Lastly, we demonstrate point-based segmentation for the humerus and ulna using the detected landmarks as inputs. Our dataset is publicly available at <https://github.com/Akahori000/Ultrasound-Medial-Elbow-Dataset>.

**Keywords:** Ultrasound Dataset, Medial Elbow, Landmark Detection, UCL injury Diagnosis, Shape Subspace

# 1 Background

## 1.1 Introduction

Ultrasound imaging is an accessible, cost-effective, and non-invasive diagnostic technique in clinical practice. In orthopedics, medial elbow ultrasound screening is commonly performed on athletes. Several studies have demonstrated that measuring the ulnohumeral joint space via ultrasound offers critical insights into the risk of Ulnar Collateral Ligament (UCL) injury [1, 2]. Specifically, an increased joint space under stress conditions indicates joint laxity and potential UCL damage. Shanley et al. [2] measured joint space by defining landmarks on the edges of the ulna and humerus in ultrasound medial elbow images. They demonstrated that pitchers with UCL injuries exhibit greater joint space compared to those without injuries ( $6.5 \pm 1.2$  mm vs  $5.3 \pm 1.2$  mm). Michinobu et al. [3] discussed optimal elbow positioning during ultrasonography to effectively diagnose joint laxity.

Several studies [4–6] have explored deep learning-based diagnosis using elbow ultrasound images. These have focused on osteochondritis dissecans or median nerve detection. However, none of the studies have discussed the automation of joint space measurement for diagnosing UCL injuries. While precise and consistent measurement is required, it is challenging due to anatomical variability, noise, and artifacts. Fig. 1(a) shows ultrasound images of the medial elbow from different participants, and Fig. 1(b) provides enlarged views of the humerus and ulna near the joint space. These images show that bone shapes vary in individuals, and bone edges are often indistinct. Also, hyperechoic lines and artifacts often appear near bone surfaces or within the joint space.

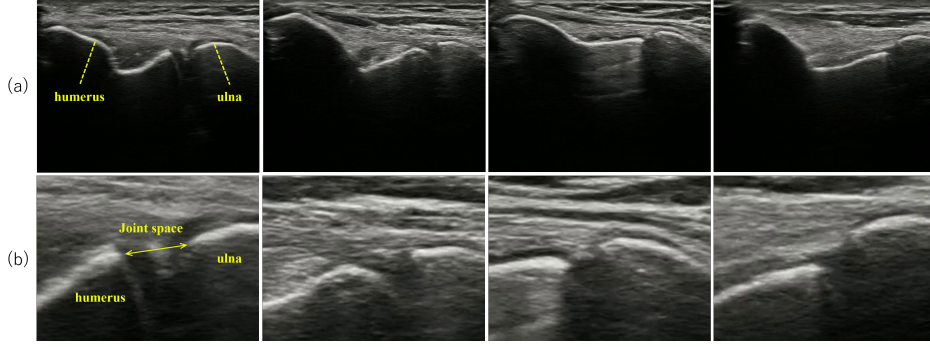


**Fig. 1** (a) The ultrasound images of the medial elbow obtained from different participants (b) The enlarged views of the joint space positions. The left and right hyperechoic lines located in the middle of each image are the humerus and ulna, respectively. The space between humerus and ulna is the joint space to be measured.

To address these challenges, training a model on a dataset of diverse joint images with accurate annotations is needed. However, no ultrasound dataset exists to measure the joint space in the medial elbow, and developing such a dataset is complex and demanding. Data acquisition requires advanced technical skills, adherence to ethical standards, and careful consideration for participants’ consent and privacy. Also, annotation requires specialized knowledge.

In this paper, we introduce a medial elbow ultrasound dataset consisting of 4,201 images from 22 individuals. The landmark annotation is made on the humerus and ulna based on the expertise of three orthopedic surgeons. We evaluated joint space measurement methods on our proposed dataset using several landmark detection approaches. While heatmap-based landmark detection methods generally achieve high accuracy, they sometimes produce multiple peaks on a heatmap, leading to incorrect detection. To mitigate this, we propose Shape Subspace landmark refinement by measuring the geometric differences between detected and reference landmark positions. The results show that our measurement method is sufficiently accurate to diagnose UCL injuries. Finally, we demonstrate point-based segmentation of the humerus and ulna using detected landmarks as inputs, showing an application of our landmark detection in the medial elbow.

## 1.2 Related works

### 1.2.1 Landmark detection

**landmark Detection Methods.** Landmark detection, known as keypoint detection, is a method of locating keypoints in images. Various methods have been proposed for pose estimation.

Regression-based approaches [7–13] directly predict landmark coordinates. While these methods are effective in simplicity and speed, they often struggle with precision in complex poses.

Heatmap-based methods overcome this by generating heatmaps where the intensity represents the likelihood of a landmark’s location, achieving better spatial accuracy.

Various studies have employed Convolutional Neural Network (CNN) including [14–25]. Among these, U-Net [24] and its extensions are widely used in localization tasks of medical images. The architecture utilizes skip connections to copy the feature maps from each stage of the encoder and directly pass them to the decoder’s corresponding stage. HRNet [25] maintains high-resolution representations throughout the whole process, allowing for accurate localization with multi-resolution features. Recently, Transformer-based approaches [26–29] have gained attention in pose estimation tasks, and these models leverage the self-attention mechanism to capture long-range dependencies to enhance precision and robustness. ViTPose [29] has a simple architecture consisting of plain Vision Transformers. Lastly, the token-based method [30, 31] learns the relationships between skeletal joints using tokens. PCT [31] designs each token to represent a substructure of joints.

**Landmark Detection in Ultrasound Images.** Several landmark detection approaches have been applied to ultrasound images to measure anatomical structures [32–36]. U-Net and its extensions are used to measure left ventricle dimensions [33, 35]. Mask R-CNN-based architecture has been employed to evaluate developmental dysplasia of the hip from infant ultrasound images [34]. HRNet-based regression architecture is proposed to assess infant growth [36].

### 1.2.2 Shape Subspace

Shape Subspace (SS) is a method to represent the 3D points of a 3D structure as a linear subspace within a high-dimensional vector space. By measuring the similarity between two shape subspaces, the geometrical difference of 3D structures can be measured [37]. Shape subspace has been utilized to classify 3D objects and human faces [38, 39].

### 1.2.3 Point-based Segmentation

Segment Anything in Images and Videos (SAM2) [40] is designed for interactive segmentation tasks, capable of processing images and videos. Using point or bounding-box prompts, SAM2 can generate accurate segmentation masks. Its robust performance is driven by a large-scale training dataset and a transformer-based architecture.

## 2 Method

### 2.1 Novel Ultrasound Elbow Dataset

#### 2.1.1 Data Collection

We constructed an ultrasound medial elbow dataset of 4,201 images from 22 participants (ages 22–56, men and women, from five countries). The images were acquired using musculoskeletal ultrasonography (SONIMAGE MX1, KONICA MINOLTA, Tokyo, Japan) with an 11-MHz linear probe by two experienced orthopedic surgeons. The participants lay on a bed with their elbows flexed at 90 degrees following [3]. Then, a surgeon moved the gel-applied probe around the medial elbow, as shown in Fig. 2(c). The images capture the medial epicondyle, UCL, medial surface of the



humeral trochlea, and coronoid process of the ulna, a key region for diagnosing medial elbow conditions [3]. The image resolution is  $528 \times 672$  pixels, corresponding to 0.0567 mm per pixel. In the images, the humerus is positioned on the left and the ulna on the right. Fig. 1 shows sample images of different participants with the enlarged joint space views.

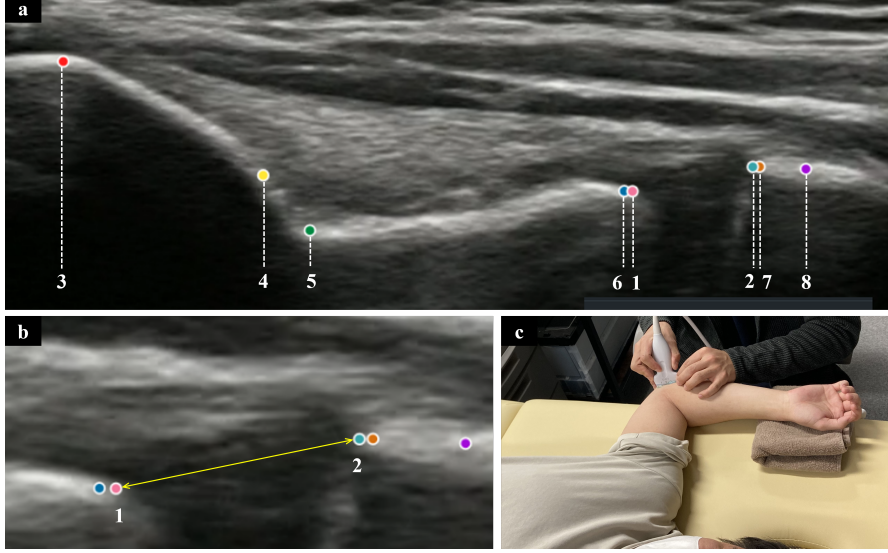


**Fig. 2** (a) The annotated landmarks: 1) Distal end of humeral trochlea, 2) Proximal end of ulnar coronoid process. Landmark 1 and 2 are the joint space measurement points. 3) Tip of humeral medial epicondyle, 4) Deep end of the intersection of humeral medial epicondyle and ulnar collateral ligament, 5) Distal end of humeral medial epicondyle, 6) Proximal point adjacent to the landmark 1 on the center of hyperechoic line of humeral trochlea, 7) Distal point adjacent to the landmark 2 on the center of hyperechoic line of ulnar coronoid process, 8) Distal point of ulnar coronoid process. The white line where landmarks 1, and 3 through 6 are located is the humerus, while the line where landmarks 2, 7, and 8 are located is the ulna. (b) The enlarged view of joint space. The yellow arrow is the joint space length to be measured. Landmark 1 and 2 are the joint space measurement points. (c) The participant's posture during the examination.

### 2.1.2 Annotation

The obtained 4,201 images were manually annotated with landmarks at sub-pixel levels by the authors under the supervision of the three orthopedic surgeons. The landmarks include two joint space measurement points: the distal end of the humeral trochlea, and the proximal end of the ulnar coronoid process, corresponding to the positions described in [2]. In addition to the joint space measurement points, six additional points on the humerus and ulna were annotated. These points are of particular interest to sonographers, who primarily focus on bone structures during ultrasound image interpretation. The annotated landmarks were meticulously reviewed and discussed by the three orthopedic experts, ensuring the reliability of the dataset.

Fig. 2(a) shows the annotated landmarks: 1) Distal end of humeral trochlea, 2) Proximal end of ulnar coronoid process. Landmark 1 and 2 are the joint space measurement points. 3) Tip of humeral medial epicondyle, 4) Deep end of the intersection of humeral medial epicondyle and ulnar collateral ligament, 5) Distal end of humeral medial epicondyle, 6) Proximal point adjacent to the landmark 1 on the center of hyperechoic line of humeral trochlea, 7) Distal point adjacent to the landmark 2 on the center of hyperechoic line of ulnar coronoid process, 8) Distal point of ulnar coronoid process. The yellow line segment between landmark 1 and 2 in Fig. 2(b) shows the joint space to be measured.

## 2.2 Landmark Detection Models

We compare several landmark detection models: HRNet [25], ViTPose [26], and U-Net [24] as heatmap-based methods, YOLOv8 [13] as a regression-based method, and PCT [31] as a token-based method.

**HRNet, ViTPose, and U-Net.** The landmark detection process of HRNet, ViTPose, and U-Net is represented in Equation 1, where  $f$  is the detection model and  $\mathbf{x} \in \mathbb{R}^{W \times H \times 3}$  is the input image with width  $W$ , height  $H$ , and 3 channels.  $f(\mathbf{x})$  outputs heatmaps of size  $W' \times H' \times K$ , where  $W'$  and  $H'$  are the heatmap dimensions, and  $K$  is the number of landmarks. The  $\arg \max(f(\mathbf{x}))$  operation returns the rough landmark coordinates  $\mathbf{p}' \in \mathbb{R}^{K \times 2}$ . The Unbiased Data Processing (UDP) function [41, 42] refines these to sub-pixel accuracy, yielding the final landmark positions  $\mathbf{p} \in \mathbb{R}^{K \times 2}$ ,  $(x, y)$  coordinates of  $K$  landmarks.

$$\mathbf{p} = \text{UDP}(\arg \max_{\mathbf{p}'}(f(\mathbf{x})), f(\mathbf{x})). \quad (1)$$

**PCT and YOLOv8.** Equation 2 represents the landmark detection using YOLOv8 and PCT.  $g$  is the landmark detection model. The output  $g(\mathbf{x}) \in \mathbb{R}^{K \times 2}$  directly predicts the coordinates of the  $K$  landmarks.

$$\mathbf{p} = g(\mathbf{x}). \quad (2)$$

## 2.3 Shape Subspace Landmark Refinement

We propose using shape subspace for landmark refinement in heatmap-based landmark detection. While heatmap-based models are trained to produce a single peak on each heatmap, they may occasionally generate multiple or unclear peaks. In such cases, measuring the geometrical similarities between detected and reference landmark positions using shape subspace can help select the most likely landmark positions. Fig. 3 provides a conceptual illustration of shape subspace landmark refinement. A shape subspace  $S$  is computed from a shape matrix  $X$  consisting of landmark coordinates which we call a point set. Then, the similarity between the two subspaces is computed.

The key advantage of using shape subspace is its ability to represent the spatial relationships of a point set, while remaining invariant under affine transformations applied to the point set. This means that the shape subspace remains unchanged in case of positional shifts of the elbow bones in the images or size differences of the bone

structures. Meanwhile, non-linear transformation of the point set, such as when the position of a point in the point set is shifted, alters the shape subspace. Although the order of the points in the shape matrices must be consistent [37], our approach always satisfies this condition because each point coordinate is obtained from each heatmap.

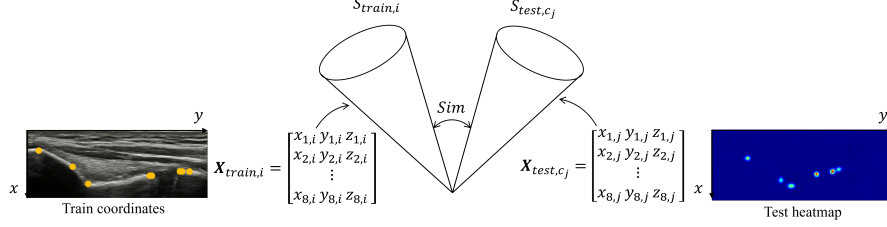


**Fig. 3** The process of shape subspace landmark refinement. Shape matrices  $\mathbf{X}_{train,i}$  and  $\mathbf{X}_{test,cj}$  are derived from the landmark coordinates of the training data and the test heatmaps, respectively. Shape subspaces  $\mathbf{S}_{train,i}$  and  $\mathbf{S}_{test,cj}$  are computed from the shape matrices, and the similarity between the two shape subspaces is compared. Note that,  $z$  in  $\mathbf{X}_{train,i}$  and  $\mathbf{X}_{test,cj}$  is set to zero to generate shape subspace from 2D coordinates.

### 2.3.1 Shape Subspace

We provide the mathematical definition of shape subspace. A shape subspace  $\mathbf{S}$  is calculated from a  $P \times 3$  shape matrix  $\mathbf{X}$  that contains 3D coordinates of an object:

$$\mathbf{X} = (\mathbf{r}_1 \mathbf{r}_2 \dots \mathbf{r}_P)^T = \begin{pmatrix} x_1 & y_1 & z_1 \\ \vdots & \vdots & \vdots \\ x_P & y_P & z_P \end{pmatrix}, \quad (3)$$

where  $\mathbf{r}_p = (x_p \ y_p \ z_p)^T$  for  $1 \leq p \leq P$  denotes the positional vector of the  $p$ -th point on an object.

Next, the shape matrix  $\mathbf{X}$  is centered, and  $\mathbf{X}_c$  is obtained to satisfy the relation  $\sum_{p=1}^P \mathbf{r}_p = 0$ , making the shape subspace invariant to affine translation of the coordinates.

$$\mathbf{X}_c = \mathbf{X} - \frac{1}{P} \sum_{p=1}^P \mathbf{r}_p. \quad (4)$$

Then, Singular Value Decomposition (SVD) of the centered matrix  $\mathbf{X}_c$  is computed, and we obtain left singular vectors  $\mathbf{U}$ , singular values  $\mathbf{\Sigma}$ , and right singular vectors  $\mathbf{V}^T$ . The basis vectors of shape subspace  $\mathbf{S}$  are defined by the first 3 columns of  $\mathbf{U}$ .

$$\mathbf{X}_c = \mathbf{U} \mathbf{\Sigma} \mathbf{V}^T. \quad (5)$$

The similarity between two shape subspaces  $\text{sim}(\mathbf{S}_1, \mathbf{S}_2)$  can be measured by the canonical angles  $\theta_i$ , where  $\{0 \leq \theta_1, \dots, \theta_N \leq \frac{\pi}{2}\}$ , and  $N = 3$ .

$$\text{sim}(\mathbf{S}_1, \mathbf{S}_2) = \frac{1}{N} \sum_{i=1}^N \cos^2 \theta_i. \quad (6)$$

Let  $\{\Phi_i\}_{i=1}^N$  be the basis vectors of  $\mathbf{S}_1$  and  $\{\Psi_i\}_{i=1}^N$  be the basis vectors of  $\mathbf{S}_2$ . The projection matrices  $\mathbf{P}_1$  and  $\mathbf{P}_2$  are calculated as:

$$\mathbf{P}_1 = \sum_{i=1}^N \Phi_i \Phi_i^T, \quad \mathbf{P}_2 = \sum_{i=1}^N \Psi_i \Psi_i^T. \quad (7)$$

$\cos^2 \theta_i$  is the  $i$ -th largest eigenvalue of  $\mathbf{P}_1 \mathbf{P}_2$  or  $\mathbf{P}_2 \mathbf{P}_1$ .

### 2.3.2 The Refinement Algorithm

First, landmark coordinate candidates are obtained from heatmaps  $f(\mathbf{x}) \in \mathbb{R}^{W' \times H' \times K}$  generated by a model. In each heatmap, up to five candidates for the landmark position are extracted. The candidates are selected in descending order based on their intensity values in the heatmap, ensuring that each candidate is at least a distance of length threshold  $L$  away from previously selected candidates to maintain spatial separation. Additionally, the values of the selected candidates must exceed the threshold of  $r\%$  of the max value in the heatmap.

Second, all possible combinations  $c_j$  of the selected landmark candidates are evaluated based on their similarities to the training data using shape subspace. Here,  $c_j$  represents the  $(x, y)$  coordinates of  $K$  landmarks, and  $\mathcal{C}$  denotes the set of all such combinations. For each combination  $c_j \in \mathcal{C}$ , its similarity to  $M$  training samples is computed, and the mean similarity is taken. Finally, the combination  $c^*$  that has the highest mean similarity is selected as follows:

$$c^* = \arg \max_{c_j \in \mathcal{C}} \left( \frac{1}{M} \sum_{i=1}^M \text{sim}(\mathbf{S}_{\text{train}, i}, \mathbf{S}_{\text{test}, c_j}) \right). \quad (8)$$

The coordinates of the selected combination  $c^*$  are then input into the UDP algorithm along with the heatmaps  $f(\mathbf{x})$ , and the refined landmark positions  $\mathbf{p}$  are obtained.

## 2.4 Point-based Bone Segmentation

We demonstrate the segmentation of the humerus and ulna using SAM2, with the detected landmarks as the point prompts.

## 2.5 Experiments

In this section, we perform landmark detection on our proposed dataset to evaluate the accuracy of joint space measurement. We assessed model performance with different landmark configurations: two-landmark detection (detecting the joint measurement points, landmark 1 and 2) and eight-landmark detection (detecting all landmarks from 1 to 8). The dataset, consisting of 4,201 images from 22 participants, was divided by individuals into 5 groups, with 3 groups used for training, 1 group for validation, and 1 group for testing, with 5-fold cross-validation.

### 2.5.1 Experimental Configuration

- **The Landmark Detection Models**

**ViTPose.** Three input image sizes were evaluated:  $256 \times 192$  pixels,  $384 \times 288$  pixels,  $512 \times 384$  pixels with corresponding output heatmap sizes of  $64 \times 48$  pixels,  $96 \times 72$  pixels,  $128 \times 96$  pixels, respectively. The augmentation process included random scaling and rotation. The Normalized Mean Error (NME) was used as the evaluation metric. The total epoch was 210, with the best epoch being selected using the validation set. The optimizer was Adam. The initial learning rate was  $1 \times 10^{-4}$ , and it was adjusted using a step-based policy, with reductions at epochs 170 and 200. The backbone was ViT-small, and the head was the classic decoder. The pre-trained model trained on ImageNet dataset was used. The patch size was  $16 \times 16$  pixels. The joint weights of all the landmarks were set to 1.0.

**HRNet.** Three input image sizes  $256 \times 192$  pixels,  $384 \times 288$  pixels,  $512 \times 384$  pixels were compared with corresponding output heatmap sizes of  $64 \times 48$  pixels,  $96 \times 72$  pixels,  $128 \times 96$  pixels, respectively. The augmentation process included random scaling and rotation. The NME was used as the evaluation metric. The total epoch was 210, with the best epoch being selected using the validation set. The optimizer was Adam. The initial learning rate was  $1 \times 10^{-4}$ , and it was adjusted using a step-based policy, with reductions at epochs 170 and 200. The backbone was HRNet-w32. The pre-trained model trained on ImageNet dataset was used. The joint weights of all the landmarks were set to 1.0.

**U-Net.** Two input image sizes  $256 \times 256$  pixels and  $512 \times 512$  pixels were used, with output heatmap sizes matching the input sizes. The augmentation process included random scaling and rotation. The normalized mean error was used as the evaluation metric. The total epoch was 600, with the best epoch selected by the validation set, and the learning rate was set to  $1 \times 10^{-3}$ .

**PCT.** Two input image sizes were evaluated:  $256 \times 256$  pixels. Data augmentation included random scaling, rotation, and shift. The Swin Transformer V2 backbone pre-trained with SimMIM on ImageNet was used. The optimizer was AdamW, with an initial learning rate of  $8 \times 10^{-4}$ , which was adjusted using a cosine annealing schedule. The number of tokens was set to 34. The training epoch was set to 50 for the tokenizer and 210 for the classifier. The joint weights of all the landmarks were set to 1.0.

**YOLOv8.** The input image size was  $640 \times 640$  pixels. The augmentation process included random rotations, scaling, shifts, and horizontal flips. Training was conducted for 1,000 epochs, with the best epoch selected for evaluation. The optimizer was AdamW for the first 10,000 iterations, followed by SGD. The initial learning rate was  $1 \times 10^{-3}$  for AdamW and  $1 \times 10^{-2}$  for SGD. The pose loss weight was set to 12.0.

- **The Number of Landmarks**

We compared two-landmark and eight-landmark detection. The two-landmark detection model detects landmarks 1 and 2. The eight-landmark model detects all

landmarks from 1 to 8. The landmark refinement is only applied to eight-landmark detection.

- **The Landmark Refinement**

The value threshold  $r$  was set to 75%, and the length threshold  $L$  was set to 5 pixels on the heatmap for the candidate selection. We used random 0.033% of the total training samples for the similarity calculation, which, for instance, corresponds to  $M = 67$ .

- **The Point Prompts for Point-based Segmentation**

We used the detected 6 points in the eight-landmark detection as the positive point prompts  $(x_i, y_i)$ , ( $i = 3, \dots, 8$ ). Also, we set the 6 negative point prompts based on the detected landmark coordinates  $(x_4, y_3)$ ,  $(x_4, y_3)$ ,  $(x_5, y_4)$ ,  $(x_5, 2y_5 - y_4)$ ,  $(x_8, 2y_5 - y_4)$ ,  $((x_1 + x_2)/2, (y_1 + y_2)/2)$ .

### 2.5.2 Evaluation Metrics

We used Mean Absolute Error (MAE) as a metric to evaluate the accuracy of each predicted landmark. Also, Euclidean Distance Error (EDE) is used to evaluate the joint space length. For metric definitions, please see the Supplementary Information.

$$\text{MAE}_k = \frac{1}{N} \sum_{i=1}^N \sqrt{(x_{i,k} - x_{i,k}^{\text{gt}})^2 + (y_{i,k} - y_{i,k}^{\text{gt}})^2}. \quad (9)$$

where  $N$  represents the total number of test samples,  $x_{j,k}$  and  $y_{j,k}$  are the predicted  $x$ - and  $y$ -coordinates of the  $k$ -th landmark in the  $i$ -th image, and  $x_{i,k}^{\text{gt}}$  and  $y_{i,k}^{\text{gt}}$  are the ground truth coordinates of the same landmark.

Also, Euclidean Distance Error (EDE) is used to evaluate the joint space length. The EDE is defined as the mean Euclidean distance error across all  $N$  samples.

$$\text{EDE} = \frac{1}{N} \sum_{i=1}^N \left| \|\mathbf{p}_{1,i} - \mathbf{p}_{1,i}\|_2 - \|\mathbf{p}_{2,i}^{\text{gt}} - \mathbf{p}_{2,i}^{\text{gt}}\|_2 \right|.$$

where  $\|\mathbf{p}_{1,i} - \mathbf{p}_{1,i}\|_2$ ,  $\|\mathbf{p}_{2,i}^{\text{gt}} - \mathbf{p}_{2,i}^{\text{gt}}\|_2$  represent the Euclidean distances for the predicted and ground truth lengths between landmarks 1 and 2, respectively.

## 3 Results

This section presents the results of the two-landmark and eight-landmark detection and point-based segmentation.

### 3.1 The Two-Landmark Detection

Table 1 displays the results for the two-landmark detection. As shown in the table, the heatmap-based methods outperformed other approaches. Among the heatmap-based methods, HRNet with an input image size of  $512 \times 384$  pixels, achieved the best performance. The average MAE for the two landmarks was 0.122, and the EDE for the joint space was 0.116 in this configuration. Fig. 4 shows the detected landmarks.

**Table 1** The two-landmark detection results. LM1 and LM2 represent the Mean Absolute Error (MAE) (mm) for landmarks 1 and 2, respectively. Ave2 is the average MAE of two landmarks. Length denotes the mean Euclidean distance error (mm) for joint space length. The bold values indicate the lowest error in each column. **Smaller values indicate better detection performance.**

Method	Input size	Joint		Ave2↓	Length↓
		LM1	LM2		
ViTPose	256×192	0.195	0.233	0.214	0.249
	384×288	0.180	0.307	0.243	0.293
	512×384	0.200	0.198	0.199	0.210
HRNet	256×192	0.187	0.227	0.207	0.221
	384×288	0.149	0.137	0.143	0.140
	512×384	<b>0.125</b>	<b>0.118</b>	<b>0.122</b>	0.116
U-Net	256×256	0.230	0.188	0.209	0.145
	512×512	0.174	0.150	0.162	<b>0.112</b>
YOLOv8	640×640	1.878	2.526	2.202	1.027
PCT	256×256	0.552	0.962	0.757	0.803

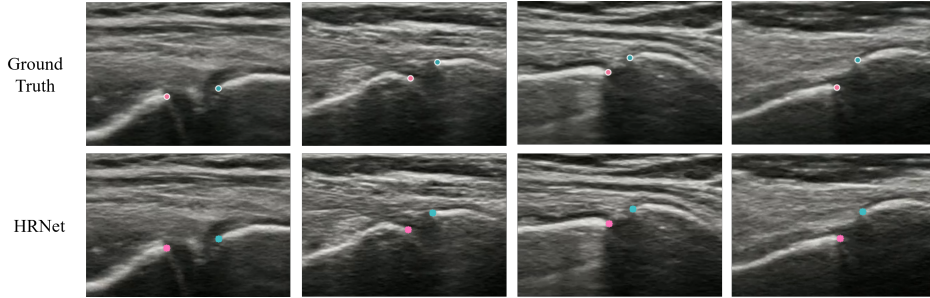


**Fig. 4** The two-landmark detection results with enlarged views around the joints. The upper row displays the ground truth and the lower row illustrates the inference results of HRNet with the input image size  $512 \times 384$ . The pink dot is landmark1, and the light blue dot is landmark2.

As illustrated in this figure, the positions of landmarks 1 and 2 are precisely detected, even in the presence of variations in bone shapes and white noise in the joint space.

### 3.2 The Eight-Landmark Detection

Table 2 presents the results for the eight-landmark detection. Among the conditions, HRNet with shape subspace landmark refinement and an input image size of  $384 \times 288$  pixels achieved the best performance across all 8 landmarks. Also, the average MAE (Ave8, Ave2) using shape subspace landmark refinement was always equal to or less than that without the refinement, indicating that shape subspace effectively refines landmark locations.

Fig. 5 illustrates the detected landmarks in the eight-landmark detection using HRNet with shape subspace refinement, showing that the landmarks are accurately located.

**Table 2** The eight-landmark detection results. LM1-LM8 represent Mean Absolute Error (MAE) (mm) for landmarks 1 through 8. Ave8 is the average MAE for all 8 landmarks (LM1–LM8), and Ave2 is the average MAE for LM1 and LM2. Length denotes the mean Euclidean distance error (mm) for joint space. SS is Shape Subspace. The bold values indicate the lowest error in each column. **Smaller values indicate better detection performance.**

Method	Input size	Joint		Humerus				Ulna		Ave8↓	Ave2↓	Length↓
		LM1	LM2	LM3	LM4	LM5	LM6	LM7	LM8			
ViTPose	256×192	0.210	0.251	0.424	0.463	0.682	0.213	0.245	0.468	0.369	0.231	0.260
	384×288	0.183	0.268	0.604	0.741	1.072	0.186	0.266	0.784	0.513	0.225	0.249
	512×384	0.237	0.344	1.205	1.164	2.147	0.237	0.323	1.003	0.833	0.291	0.322
ViTPose+SS	256×192	0.210	0.251	0.427	0.463	<b>0.674</b>	0.213	0.245	0.468	0.369	0.231	0.260
	384×288	0.183	0.259	0.566	0.608	0.798	0.186	0.258	0.594	0.432	0.221	0.245
	512×384	0.201	0.303	0.881	0.971	1.315	0.218	0.262	0.697	0.606	0.252	0.285
HRNet	256×192	0.184	0.251	0.458	<b>0.453</b>	0.774	0.184	0.245	0.495	0.381	0.218	0.239
	384×288	0.171	0.183	0.411	0.459	0.781	0.171	0.175	0.472	0.353	0.177	0.185
	512×384	<b>0.148</b>	<b>0.154</b>	0.495	0.529	0.976	<b>0.152</b>	<b>0.147</b>	0.471	0.384	<b>0.151</b>	0.158
HRNet+SS	256×192	0.184	0.251	0.458	<b>0.453</b>	0.774	0.184	0.245	0.495	0.381	0.218	0.239
	384×288	0.171	0.182	<b>0.383</b>	0.459	0.771	0.171	0.174	0.472	<b>0.348</b>	0.176	0.183
	512×384	<b>0.148</b>	<b>0.154</b>	0.419	0.528	0.844	<b>0.152</b>	0.148	<b>0.468</b>	0.358	<b>0.151</b>	0.158
U-Net	256×256	0.202	0.164	0.691	1.000	1.163	0.207	0.163	0.482	0.509	0.183	<b>0.141</b>
	512×512	0.175	0.173	5.556	1.666	3.326	0.180	0.148	0.698	1.490	0.174	0.150
YOLOv8	640×640	0.585	0.717	0.677	0.540	0.717	0.587	0.710	1.837	0.796	0.651	0.718
PCT	256×256	0.640	0.954	1.087	0.655	1.235	0.623	0.941	1.035	0.896	0.797	0.585

### 3.3 Point-based Segmentation

Fig. 6 shows the point-based segmentation results using SAM2 with point prompts derived from HRNet-detected landmarks and shape subspace refinement. The green stars indicate positive prompts, the red stars denote negative prompts, and the blue areas represent segmented regions. This figure shows that the humerus and ulna are segmented with high fidelity.

## 4 Discussion

First, heatmap-based methods outperformed other approaches in both results. Among them, HRNet achieved the highest performance. The ability of HRNet to capture local features while maintaining high-resolution representations can make it suitable for precise landmark detection in ultrasound images. In contrast, Transformer-based models like ViTPose typically require larger datasets for effective training. Given the limited dataset size, HRNet’s efficiency with smaller datasets appears to contribute to its superior performance.

Second, the two-landmark detection demonstrated better accuracy in joint space measurements than the eight-landmark detection model. This is likely because the simpler task of detecting fewer landmarks allows the model to focus on the most relevant features.



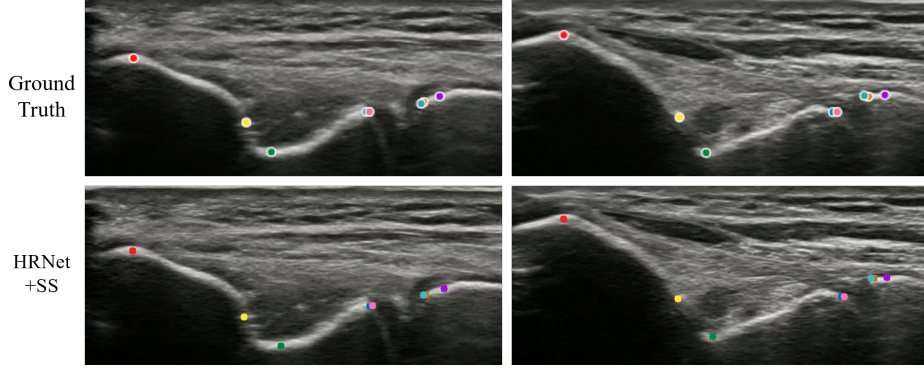


**Fig. 5** The eight-landmark detection results with enlarged views around the joints. The first row shows the ground truth for 8 landmarks. The second row illustrates the positions of detected landmarks by HRNet+SS with the input size  $384 \times 288$ . The colors of landmarks 1 to 8 are pink, light blue, red, yellow, green, blue, orange, and purple.

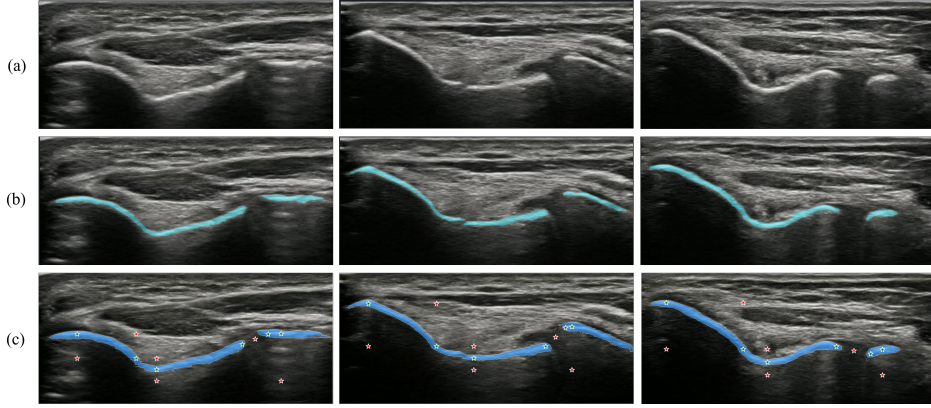


**Fig. 6** The point-based segmentation results using SAM2 with the point prompts calculated by the detected landmark positions. (a) The original images, (b) The ground truth of the bone segmentation. (c) The segmented images using SAM2 and the point prompts calculated from detected landmarks. The blue areas represent the segmented regions, the green stars indicate the positive point prompts and the red stars denote the negative point prompts.

Third, in the eight-landmark model, shape subspace refined landmark positions. Fig. 7 displays a refinement example, with the LM3 heatmap having multiple peaks. Although the right peak has a higher value than the left peak in the LM3, the shape subspace refinement correctly selects the left peak that aligns with the ground truth position of landmark 3, as shown by the red point on Fig. 7(b).

Fig. 8 shows the relative error after applying shape subspace landmark refinement. As the ratio of multiple peaks in the heatmaps increases, the MAE decreases, demonstrating the effectiveness of shape subspace refinement. The refinement was more pronounced in ViTPose, likely because its broader context capture produces multiple peaks in heatmaps more frequently.

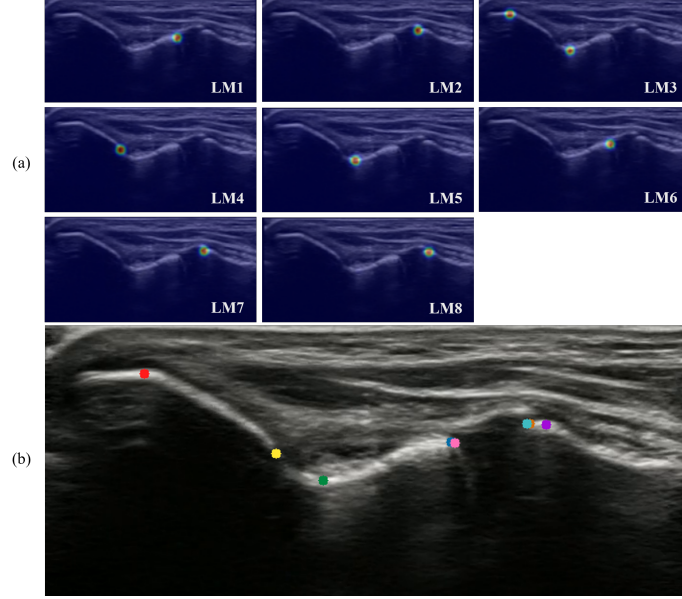


**Fig. 7** An example of landmark refinement using shape subspace. (a) shows overlays of the output heatmaps on the input image. In the LM3 heatmap, multiple peaks are observed, with the right peak exhibiting higher intensity. However, shape subspace refinement correctly selects the left peak, which more accurately aligns with the ground truth. (b) displays the detected landmarks, where the red point represents the initial position obtained from LM3. The detected landmarks 1–8 are shown in pink, light blue, red, yellow, green, blue, orange, and purple, respectively.

Finally, our method satisfy the accuracy needed for UCL injury diagnosis. While pitchers with UCL injuries show an average joint space increase of 1.2 mm [2], our method achieved a 0.116 mm average error using HRNet in two-landmark detection.

**Limitation.** First, the dataset was acquired using specific ultrasound equipment, which may not fully capture clinical variability. Second, despite the dataset comprising data from participants from diverse backgrounds, the model may have limited generalization to populations with different anatomies. Third, while shape subspace refines landmarks when multiple peaks exist, it may struggle when peaks are closely connected.

## 5 Conclusion

In this paper, we introduced a novel ultrasound dataset consisting of 4,201 medial elbow images from 22 individuals, annotated with landmarks under the supervision of orthopedic experts. We evaluated joint space measurement methods on our dataset using multiple landmark detection models. The results showed that HRNet achieved a mean joint space measurement error of 0.116 mm, demonstrating sufficient precision for detecting UCL injuries. In addition, we proposed a shape subspace landmark refinement method, which improved landmark localization performance. These suggest that our approach can facilitate the early diagnosis and intervention of UCL injuries by

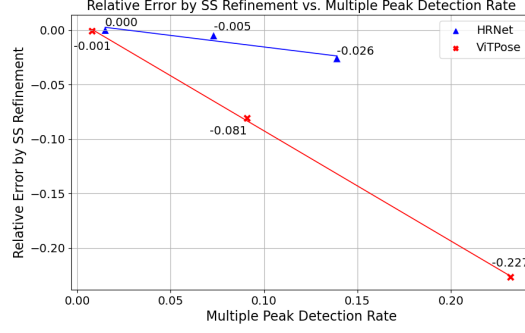


**Fig. 8** The relative error when shape subspace (SS) landmark refinement is applied. The relative error by SS refinement represents the change in the mean absolute error (MAE) of all the landmarks when the shape subspace is applied in the 8-landmark detection task. Multiple peak detection rate indicates the ratio of test samples with multiple peaks in at least one heatmap. Each plot corresponds to a different input image size. As the multiple peak detection rate in the heatmap increases, the MAE decreases.

enabling automated joint space measurement. Furthermore, we demonstrated point-based bone segmentation of the humerus and ulna using detected landmarks as point prompts, highlighting a potential application of our dataset and methodology in musculoskeletal ultrasound analysis.

## 6 Declarations and Statements

### 6.1 Competing Interests

The authors declare no competing interests.

### 6.2 Funding

This study is supported by [Blinded for review].

### 6.3 Ethics Approval

This study complies with the 1964 Declaration of Helsinki. Approval was obtained by a committee of [Blinded for review].

### 6.4 Consent to Participate

Written consent was obtained from all participants.

### 6.5 Informed Consent and Consent for Publication

Not applicable. The ultrasound images used for this study do not contain personally identifiable information.

## 6.6 Data Availability Statement

The dataset is available at <https://github.com/Akahori000/Ultrasound-Medial-Elbow-Dataset>.

## References

- [1] Ciccotti, M.G., Atanda, A., Nazarian, L.N., Dodson, C.C., Holmes, L., Cohen, S.B.: Stress sonography of the ulnar collateral ligament of the elbow in professional baseball pitchers: A 10-year study. *The American Journal of Sports Medicine* **42**(3), 544–551 (2014) <https://doi.org/10.1177/0363546513516592>
- [2] Shanley, E., Smith, M., Mayer, B.K., Bailey, L.B., Thigpen, C.A., Tokish, J.M., Kissenberth, M.J., Noonan, T.J.: Using stress ultrasonography to understand the risk of ucl injury among professional baseball pitchers based on ligament morphology and dynamic abnormalities. *Orthopaedic Journal of Sports Medicine* **6**(8) (2018) <https://doi.org/10.1177/2325967118788847>
- [3] Michinobu, R., Ogawa, T., Yoshii, Y., Ikumi, A., Ikeda, K., Tsuge, H., Teruya, S., Hara, Y., Yamazaki, M.: Optimal limb position for the stress ultrasound evaluation of elbow valgus laxity in baseball players. *Orthopaedic Journal of Sports Medicine* **12**(2) (2024) <https://doi.org/10.1177/23259671231221523>
- [4] Inui, A., Mifune, Y., Nishimoto, H., Mukohara, S., Fukuda, S., Kato, T., Furukawa, T.a., Tanaka, S., Kusunose, M., Takigami, S., Ehara, Y., Kuroda, R.: Detection of elbow ocd in the ultrasound image by artificial intelligence using yolov8. *Applied Sciences* **13**(13) (2023) <https://doi.org/10.3390/app13137623>
- [5] Sasaki, K., Fujita, D., Takatsuji, K., Kotoura, Y., Minami, M., Kobayashi, Y., Sukenari, T., Kida, Y., Takahashi, K., Kobashi, S.: Deep learning-based osteochondritis dissecans detection in ultrasound images with humeral capitellum localization. *International Journal of Computer Assisted Radiology and Surgery* (2024) <https://doi.org/10.1007/s11548-023-03040-8>
- [6] Gujarati, K.R., Bathala, L., Venkatesh, V., Mathew, R.S., Yalavarthy, P.K.: Transformer-based automated segmentation of the median nerve in ultrasound videos of wrist-to-elbow region. *IEEE Transactions on Ultrasonics, Ferroelectrics, and Frequency Control* **71**(1), 56–69 (2024) <https://doi.org/10.1109/TUFFC.2023.3330539>
- [7] Toshev, A., Szegedy, C.: Deeppose: Human pose estimation via deep neural networks. In: *Proceedings of the IEEE Conference on Computer Vision and Pattern Recognition (CVPR)* (2014)
- [8] Carreira, J., Agrawal, P., Fragkiadaki, K., Malik, J.: Human pose estimation with iterative error feedback. In: *2016 IEEE Conference on Computer Vision and Pattern Recognition (CVPR)*, pp. 4733–4742. IEEE Computer Society, Los

- Alamitos, CA, USA (2016). <https://doi.org/10.1109/CVPR.2016.512>
- [9] Liang, S., Sun, X., Wei, Y.: Compositional human pose regression. *Computer Vision and Image Understanding* **176-177**, 1–8 (2018) <https://doi.org/10.1016/j.cviu.2018.10.006>
  - [10] Geng, Z., Sun, K., Xiao, B., Zhang, Z., Wang, J.: Bottom-up human pose estimation via disentangled keypoint regression. In: 2021 IEEE/CVF Conference on Computer Vision and Pattern Recognition (CVPR), pp. 14671–14681. IEEE Computer Society, Los Alamitos, CA, USA (2021). <https://doi.org/10.1109/CVPR46437.2021.01444>
  - [11] Li, J., Bian, S., Zeng, A., Wang, C., Pang, B., Liu, W., Lu, C.: Human pose regression with residual log-likelihood estimation. In: *Proceedings of the IEEE/CVF International Conference on Computer Vision (ICCV)*, pp. 11025–11034 (2021)
  - [12] Wang, C.-Y., Bochkovskiy, A., Liao, H.-Y.M.: Yolov7: Trainable bag-of-freebies sets new state-of-the-art for real-time object detectors. In: 2023 IEEE/CVF Conference on Computer Vision and Pattern Recognition (CVPR), pp. 7464–7475 (2023). <https://doi.org/10.1109/CVPR52729.2023.00721>
  - [13] Jocher, G., Chaurasia, A., Qiu, J.: YOLOv8 (2023). <https://github.com/ultralytics/ultralytics>
  - [14] Tompson, J., Jain, A., LeCun, Y., Bregler, C.: Joint training of a convolutional network and a graphical model for human pose estimation. In: *Proceedings of the 27th International Conference on Neural Information Processing Systems - Volume 1*, pp. 1799–1807. MIT Press, Cambridge, MA, USA (2014)
  - [15] Wei, S., Ramakrishna, V., Kanade, T., Sheikh, Y.: Convolutional pose machines. In: 2016 IEEE Conference on Computer Vision and Pattern Recognition (CVPR), pp. 4724–4732. IEEE Computer Society, Los Alamitos, CA, USA (2016). <https://doi.org/10.1109/CVPR.2016.511>
  - [16] Newell, A., Yang, K., Deng, J.: Stacked hourglass networks for human pose estimation. In: Leibe, B., Matas, J., Sebe, N., Welling, M. (eds.) *Computer Vision – ECCV 2016*, pp. 483–499. Springer, Cham (2016)
  - [17] Bulat, A., Tzimiropoulos, G.: Human pose estimation via convolutional part heatmap regression. In: Leibe, B., Matas, J., Sebe, N., Welling, M. (eds.) *Computer Vision – ECCV 2016*, pp. 717–732. Springer, Cham (2016)
  - [18] Newell, A., Huang, Z., Deng, J.: Associative embedding: end-to-end learning for joint detection and grouping. In: *Proceedings of the 31st International Conference on Neural Information Processing Systems. NIPS’17*, pp. 2274–2284. Curran Associates Inc., Red Hook, NY, USA (2017)

- [19] Yang, W., Li, S., Ouyang, W., Li, H., Wang, X.: Learning feature pyramids for human pose estimation. In: 2017 IEEE International Conference on Computer Vision (ICCV), pp. 1290–1299 (2017). <https://doi.org/10.1109/ICCV.2017.144>
- [20] Cao, Z., Hidalgo, G., Simon, T., Wei, S., Sheikh, Y.: Openpose: Realtime multi-person 2d pose estimation using part affinity fields. *IEEE Transactions on Pattern Analysis and Machine Intelligence* **43**(01), 172–186 (2021) <https://doi.org/10.1109/TPAMI.2019.2929257>
- [21] Chen, Y., Wang, Z., Peng, Y., Zhang, Z., Yu, G., Sun, J.: Cascaded pyramid network for multi-person pose estimation. In: *Proceedings of the IEEE Conference on Computer Vision and Pattern Recognition (CVPR)* (2018)
- [22] Cheng, B., Xiao, B., Wang, J., Shi, H., Huang, T.S., Zhang, L.: Higherhrnet: Scale-aware representation learning for bottom-up human pose estimation. In: 2020 IEEE/CVF Conference on Computer Vision and Pattern Recognition (CVPR), vol. 1, pp. 5385–5394 (2020). <https://doi.org/10.1109/CVPR42600.2020.00543>
- [23] Zhang, F., Zhu, X., Dai, H., Ye, M., Zhu, C.: Distribution-aware coordinate representation for human pose estimation. In: 2020 IEEE/CVF Conference on Computer Vision and Pattern Recognition (CVPR), pp. 7091–7100 (2020)
- [24] Ronneberger, O., Fischer, P., Brox, T.: U-net: Convolutional networks for biomedical image segmentation. In: Navab, N., Hornegger, J., Wells, W.M., Frangi, A.F. (eds.) *Medical Image Computing and Computer-Assisted Intervention – MICCAI 2015*, pp. 234–241. Springer, Cham (2015)
- [25] Wang, J., Sun, K., Cheng, T., Jiang, B., Deng, C., Zhao, Y., Liu, D., Mu, Y., Tan, M., Wang, X., Liu, W., Xiao, B.: Deep high-resolution representation learning for visual recognition. *IEEE Transactions on Pattern Analysis and Machine Intelligence* **43**(10), 3349–3364 (2021) <https://doi.org/10.1109/TPAMI.2020.2983686>
- [26] Su, K., Yu, D., Xu, Z., Geng, X., Wang, C.: Multi-person pose estimation with enhanced channel-wise and spatial information. In: 2019 IEEE/CVF Conference on Computer Vision and Pattern Recognition (CVPR), pp. 5667–5675 (2019). <https://doi.org/10.1109/CVPR.2019.00582>
- [27] Yang, S., Quan, Z., Nie, M., Yang, W.: Transpose: Keypoint localization via transformer. In: 2021 IEEE/CVF International Conference on Computer Vision (ICCV), pp. 11782–11792 (2021). <https://doi.org/10.1109/ICCV48922.2021.01159>
- [28] Yuan, Y., Fu, R., Huang, L., Lin, W., Zhang, C., Chen, X., Wang, J.: Hrformer: High-resolution vision transformer for dense predict. In: Ranzato, M., Beygelzimer, A., Dauphin, Y., Liang, P.S., Vaughan, J.W. (eds.) *Advances in Neural Information Processing Systems*, vol. 34, pp. 7281–7293 (2021)

- [29] Xu, Y., Zhang, J., Zhang, Q., Tao, D.: Vitpose: simple vision transformer baselines for human pose estimation. In: Proceedings of the 36th International Conference on Neural Information Processing Systems. NIPS '22. Curran Associates Inc., Red Hook, NY, USA (2024)
- [30] Li, W., Wang, Z., Yang, S., Liu, Y., Yang, W., Xu, X., Gao, Y.: Tokenpose: Learning keypoint tokens for human pose estimation. arXiv preprint arXiv:2104.03516 **2021**, 1293–1301 (2021) <https://doi.org/10.1109/ICCV48922.2021.00129>
- [31] Geng, Z., Wang, C., Wei, Y., Liu, Z., Li, H., Hu, H.: Human pose as compositional tokens. In: Proceedings of the IEEE/CVF Conference on Computer Vision and Pattern Recognition (CVPR), pp. 660–671 (2023)
- [32] Kanauchi, Y., Hashimoto, M., Toda, N., Okamoto, S., Haque, H., Jinzaki, M., Sakakibara, Y.: Automatic detection and measurement of renal cysts in ultrasound images: A deep learning approach. *Healthcare (Basel)* **11**(4), 484 (2023) <https://doi.org/10.3390/healthcare11040484>
- [33] Gilbert, A., Holden, M., Eikvil, L., Aase, S.A., Samset, E., McLeod, K.: Automated left ventricle dimension measurement in 2d cardiac ultrasound via an anatomically meaningful cnn approach. In: Smart Ultrasound Imaging and Perinatal, Preterm and Paediatric Image Analysis: First International Workshop, SUSI 2019, and 4th International Workshop, PIPPI 2019, Held in Conjunction with MICCAI 2019, Shenzhen, China, October 13 and 17, 2019, Proceedings, pp. 29–37. Springer, Berlin, Heidelberg (2019). [https://doi.org/10.1007/978-3-030-32875-7\\_4](https://doi.org/10.1007/978-3-030-32875-7_4)
- [34] Hu, X., Wang, L., Yang, X., Zhou, X., Xue, W., Cao, Y., Liu, S., Huang, Y., Guo, S., Shang, N., Ni, D., Gu, N.: Joint landmark and structure learning for automatic evaluation of developmental dysplasia of the hip. *IEEE Journal of Biomedical and Health Informatics* **26**, 345–358 (2021)
- [35] Jafari, M.H., Girgis, H., Van Woudenberg, N., Liao, Z., Rohling, R., Gin, K., Abolmaesumi, P., Tsang, T.: Automatic biplane left ventricular ejection fraction estimation with mobile point-of-care ultrasound using multi-task learning and adversarial training. *International Journal of Computer Assisted Radiology and Surgery* **14**(6), 1027–1037 (2019) <https://doi.org/10.1007/s11548-019-01954-w>
- [36] Avidris, N., Joskowicz, L., Dromey, B., David, A.L., Peebles, D., Stoyanov, D., Bashat, D.B., Bano, S.: Biometrynet: Landmark-based fetal biometry estimation from standard ultrasound planes. In: International Conference on Medical Image Computing and Computer-Assisted Intervention (2022)
- [37] Igarashi, Y., Fukui, K.: 3d object recognition based on canonical angles between shape subspaces. In: Kimmel, R., Klette, R., Sugimoto, A. (eds.) *Computer Vision – ACCV 2010*, pp. 580–591. Springer, Berlin, Heidelberg (2011)



- [38] Yoshinuma, T., Hino, H., Fukui, K.: Personal authentication based on 3d configuration of micro-feature points on facial surface. In: Bräunl, T., McCane, B., Rivera, M., Yu, X. (eds.) *Image and Video Technology*, pp. 433–446. Springer, Cham (2016)
- [39] Yataka, R., Fukui, K.: Three-dimensional object recognition via subspace representation on a grassmann manifold. In: *International Conference on Pattern Recognition Applications and Methods* (2017)
- [40] Ravi, N., Gabeur, V., Hu, Y.-T., Hu, R., Ryali, C., Ma, T., Khedr, H., Rädle, R., Rolland, C., Gustafson, L., Mintun, E., Pan, J., Alwala, K.V., Carion, N., Wu, C.-Y., Girshick, R., Dollár, P., Feichtenhofer, C.: Sam 2: Segment anything in images and videos. *arXiv preprint arXiv:2408.00714* (2024)
- [41] Huang, J., Zhu, Z., Guo, F., Huang, G.: The devil is in the details: Delving into unbiased data processing for human pose estimation. In: *Proceedings of the IEEE/CVF Conference on Computer Vision and Pattern Recognition (CVPR)* (2020)
- [42] Zhang, F., Zhu, X., Dai, H., Ye, M., Zhu, C.: Distribution-aware coordinate representation for human pose estimation. In: *Proceedings of the IEEE/CVF Conference on Computer Vision and Pattern Recognition (CVPR)* (2020)